applied sciences

MDPI

Article

Numerical Evaluation in a Scaled Rotor-Less Nozzle Vaned Radial Turbine Model under Variable Geometry Conditions

José Ramón Serrano [1], Andrés Omar Tiseira [1], Juan Antonio López-Carrillo [1,*] and Natalia Hervás-Gómez [2]

[1] CMT-Motores Térmicos, Universitat Politécnica de Valéncia, 46022 Valencia, Spain; jrserran@mot.upv.es (J.R.S.); anti1@mot.upv.es (A.O.T.)
[2] Sistemas Para Capturar y Normalizar S.L.U., 46550 Valencia, Spain; nahergme@mot.upv.es
* Correspondence: jualoca6@mot.upv.es

Abstract: The widespread trend of pursuing higher efficiencies in radial turbochargers led to the prompting of this work. A 3D-printed model of the static parts of a radial variable geometry turbine, the vaned nozzle, and the volute, was developed. This model was up-scaled from the actual reference turbine to place sensors and characterize the flow around the nozzle vanes, including the tip gap. In this study, a computational model of the scaled-up turbine was carried out to verify the results in two ways. For this model, firstly compared with an already validated CFD turbine model of the real device (which includes a rotor), its operating range was extended to different nozzle positions, and we checked the issues with rotor–stator interactions as well as the influence of elements such as the screws of the turbine stator. After showing results for different nozzle openings, another purpose of the study was to check the effect of varying the clearance over the tip of the stator vanes on the tip leakage flow since the 3D-printed model has variable gap height configurations.

Keywords: turbocharger; radial turbine; CFD analysis; nozzle vane; variable geometry turbine

Citation: Serrano, J.R.; Tiseira, A.O.; López-Carrillo, J.A.; Hervás-Gómez, N. Numerical Evaluation in a Scaled Rotor-Less Nozzle Vaned Radial Turbine Model under Variable Geometry Conditions. *Appl. Sci.* **2022**, *12*, 7254. https://doi.org/10.3390/app12147254

Academic Editor: Cesare Biserni

Received: 28 June 2022
Accepted: 15 July 2022
Published: 19 July 2022

1. Introduction

Reciprocating engines applied to means of transport represent about 23% of the CO_2 generated by means of transport worldwide [1]. Over the last decades, the European Standard on pollution emissions has been significantly toughened [2,3]. Today's engines are not in the list of engines to be admitted in the near future. Therefore, to comply with the exhaust emissions limits defined by the European Union (EU), engine manufacturers have approached the situation in two different ways: treating the pollution emission generated during combustion [4–8], which can have some problems, such as urea injection failures which is treated in [9], and trying to reduce these emissions via hybridization and increasing the combustion thermal efficiency. Increased thermal efficiency can be achieved by supercharging [10–13]. The aim of supercharging is to increase intake air pressure which means rising volumetric efficiency and allow downsizing engines [14].

Several researchers have proven that the use of turbochargers improves the engine power and combustion efficiency, meanwhile reducing pollutant emissions regardless of the fuel used [15]. Hence, current research lines look for cleaner fuels without pollutant emissions. The new so-called "pollution-free" engines will run on a hydrogen-based fuel and will continue to require turbochargers to achieve the power and torque performance of their polluting predecessors due to the low density of hydrogen (indirect injection) [16] or to reduce NOx emissions (direct injection) [17].

In any case, engines will be smaller, combined or not with new alternatives such as the use of non-polluting synthetic fuels, electric motors, or fuel cells. Regardless of new environmentally friendly propulsion systems introduced in either land, water, or air conveyance, turbocharging is still part of the new alternatives [18], except for purely electric ones, which cannot cope with many applications and transport demands, according to some experts [19].

Commonly, the expansion stage in small-size turbochargers is composed of a radial turbine which counts a volute, a stator, and a rotor. The function of the first two elements is to condition the flow at the rotor inlet efficiently so that it transforms kinetic energy into mechanical energy to move the centrifugal compressor at the engine intake. The volute and stator geometry design can compromise the fluid behavior, and this is key for the rotor to achieve better efficiencies, something which authors such as [20] have researched. For this reason, the stator can have, in some turbines, movable vanes that control and adapt the flow depending on the operating conditions. These variable geometry nozzles in the stator help to extend the operating range of the turbine; meanwhile, the matching with the compressor side can be achieved by the use of a ported shroud [21]. Uniform distribution over the 360 degrees of the radial stator is important to then adapt the flow at the rotor inlet, a matter of interest in [22], where they tested flow behavior for twin-entry turbines as two separated single VGT volutes. Therefore, while some authors focus on a volute casing optimization, as in [23], the stator and its vanes must be designed according to an aerodynamic geometry that has the least possible amount of energy losses [24–26].

Conventional design criteria for each turbine part (volute, stator, and rotor) focus primarily on ideal gas, but new systems under development such as hydrogen or industrial gases, such as S-CO_2, require further research on radial turbines [27]. The use of new propulsion systems, alternative to diesel and gasoline engines, need to have a turbocharging system suitable for their needs; therefore, work on these geometries is still in progress in multiple areas. There are many challenges to overcome with these kind of turbines, especially when they are attached to a compressor and the variable operating conditions could lead to undesirable consequences, as it could be the mistuned bladed disc effect, treated by several authors [28,29]. Internal flow is a high-interest research area which is producing multiple articles in different fields of study: in the case of [30], the phenomena of compressibility is analyzed, alongside the areas where there is greater incidence of shock waves with different nozzle openings. Authors from [31] have developed high-order models for radial turbines. On the other hand, in [32], an up-scaled experimental turbine model was presented. This model allows the study and characterization of the internal flow through the nozzle channels thanks to its size, which enables the use of instrumentation that normally does not fit in real-sized turbomachinery, limiting the possibilities to set few probes, as in [33], or as in [34], although they place the probes in the rotor clearance. The use of this experimental tool will provide useful information for the evolution and adaptation of the turbines to the new propulsion systems. However, the validation of this tool was performed just for a VGT opening, a gap height of the vane, and flow conditions. Due to the large operating range that currently represents turbochargers, this validation may have limited results.

Therefore, this work focuses on validating, through numerical simulations, a vaned stator scale mock-up for a set of stator geometries and flow conditions that comprehensively demonstrate their utility throughout the turbine operating range. The intention is then to check if studying the stator in a rotor-less turbine is analogue to doing so in a conventional one, foreseeing the future experimental studies on the printed model. Consequently, this article first describes geometries and operating conditions under study. Next, it shows the mesh analysis carried out for the set of studied geometries and compares it with a reference one, which is already validated. Following this, an analysis on the flow applied to the different cases in the study is presented. Likewise, the validation was extended with numerous results. Finally, the limitations for the validity of the up-scaled model are listed. With those results, the convenience of performing experimental tests on the printed mock-up as representative of the behavior in a conventional radial turbine is set.

2. Materials and Methods

To extend the validation of the scaled model for the whole operating range of the turbine, different vane openings are simulated. The validation of these simulations on the scaled turbine (ST) comes from [35], where a CFD code of the real-sized turbine (RT)

was compared to experimental results. Flow behavior through the volute and the stator is compared between ST and RT. After comparing the two models, a variation in gap height for ST is also simulated. The printed model that motivated this research was designed with a modular structure, consisting of vanes with different heights and openings, as shown in Figure 1. The geometry model developed is scaled in a 3:1 proportion, looking for a trade-off between having as much space as possible for measuring instrumentation and fitting the experimental test rig and its experimental conditions. Geometry specifications of both the scaled and real turbine stator can be seen in Table 1. The scaled model has two different clearance heights over the stator tip. The 0.5 mm height is used to validate the ST model since its tip-to-blade height ratio is equal to the RT one. Meanwhile, the 1.5 mm height is an additional study on how the tip leakage works with different gaps.

Figure 1. Printed nozzles with different vanes position.

Table 1. Geometry specifications.

	Scaled Turbine (ST)	**Real Turbine (RT)**
Blade number	11	11
Chord length	52.5 mm	17.5 mm
Vane height	24 mm	8 mm
Tip height	1.5 and 0.5 mm	0.2 mm
Tip-to-vane ratio	0.063 and 0.021	0.025
Blade angle-α	51° 65° 73°	53° 63° 73°
VGT opening	80% 60% 30%	60% 30%

Thus, the geometry used for CFD simulations comes directly from the CAD of the printed model, where two vane openings are studied (VGT30 and VGT60). A feature of interest is the fact that in the printed model, it was decided to remove three screws that existed in RT to study an ideal situation for every channel between vanes. Hence, information regarding the losses due to those screws is depicted for different vane openings.

2.1. CFD Setup

The configuration of the CFD model, using STAR-CCM+ 14.02.010, starts by setting fluid properties, selecting air that is modeled as an ideal gas. This assumption is valid due to the low variation of static temperature in the studied cases through the rotor-less turbine. The simulation is set as a steady-state case, and the turbulence is modeled with an RANS k-ω SST model. This model has been extensively used in turbomachinery by authors such as Smirnov et al. or Galindo et al., due to its behavior when adverse pressure gradients and flow separation are present. Additionally, the inlet turbulence intensity was set with a value of 4%. A coupled implicit solver was set with a controlled CFL number to ensure stability. Furthermore, as the CFD case used for the validation is adiabatic, every wall in the domain possesses adiabatic conditions. In every wall, the option of non-slip boundary condition is enabled to consider wall friction. Besides the boundary condition of each solid wall, at the inlet region, where the duct begins, mass flow inlet condition was

set, adding a total inlet temperature that fits with the test bench capacities. On the other hand, at the outlet section, static pressure was imposed with atmospheric conditions since the experimental setup was designed that way.

For turbomachinery applications, it is crucial to obtain information on how the fluid behaves within the so-called nozzle vanes or blades when referring to the impeller. The regions composing the inner volume of the turbine, that is, volute, stator, and the place where the rotor would have been normally placed (but avoided in this design), are meshed with a unstructured polyhedral one, as shown in Figure 2a. Apart from that, inlet and outlet regions, built by extruding the corresponding sections at the intake and the outlet of the turbine, include an extruded mesh. The growth of notorious gradients in the boundary layer or separation bubbles on the stator vanes involve using a prism layer meshing strategy in the near-wall region (as shown in the vane-surrounding region in Figure 2b). A logarithmic function is implemented with the effect of having a higher cell density near the walls. A constant growth rate is applied in the normal direction to the wall until the chosen base cell size is reached in the free stream region. The size of the first cell at the wall must be selected according to the required level of accuracy for viscous effects, being thinner than the viscous sublayer, according to Dufour et al. [36]. Another value to be considered is the dimensionless wall distance y^+ that, when using the k-ω SST model, is recommended to have values $y^+ < 2$, according to Menter et al. [37]. However, this value can be enlarged if the complexity of the flow requires it.

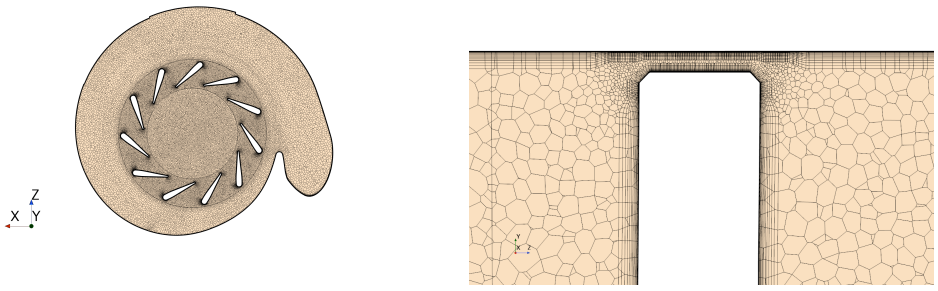

(**a**) (**b**)

Figure 2. Polyhedral unstructured mesh with refinements near walls. (**a**) Mesh upper view. (**b**) Prism layer meshing surrounding vanes.

A mesh convergence analysis was carried out to obtain the most appropriate cell number, the least without interacting with the solution. A variation in the base size and the total number of cells in the prism layer meshing was performed. As previously stated, we were looking for a low Reynolds mesh.

2.2. 1D Model

Analogies were used to ensure similarity between RT and ST when validating ST using the 0.5 mm gap height because of the 3:1 proportion scale on these models. Two different similarities were used; on the one hand, Mach, and on the other hand, Reynolds similarity were set. When searching for a lookalike Mach distribution in the stator, a similar blade loading was expected to appear. When chasing the same Reynolds number, the same patterns of flow near walls are expected to be found. This is detachment and separation in the boundary layer. Thus, Reynolds similarity would be more appropriate to study the tip leakage flow through the gap since it is a region highly affected by wall effects.

Since the operating points in the real turbine have to fulfill the requirements to meet the aforementioned similarities, the scaled model defines the reference operating point. A point with the highest pressure and mass flow that the experimental test bench can supply was chosen since that would be the one tested by the 3D model scaled turbine when the experimental campaign would take place. The decision to apply the maximum of these parameters (pressure and mass flow) is based on the fact that the viscous effects and flow separation are more notorious at this point.

Due to the Mach similarity, both static and absolute values can be compared indistinctly. The increase of density derived from the highest pressure resulted in reducing mass flow. Regarding the temperature imposed for the simulations, quasi-adiabatic measurements are widely used in research, having relatively low temperatures at the inlet. In addition, some authors, such as Baar et al. [38] and Zimmermann et al. [39], demonstrated that the reduced mass flow map of the turbine offered the same efficiency for hot and cold temperatures through adiabatic measurements. The materials of the printed model and the instrumentation that would be employed when the experimental campaign is performed are not designed to endure such high temperatures. For that reason, the inlet temperature of the turbine is set in the model at 343.15 K. This boundary condition is ubiquitous independently of the VGT opening or the similarity studied. This temperature was similar to the obtained values in the experiments performed over the real turbine by Serrano et al. [40] in the quasi-adiabatic experiments and simulations.

Two studies were performed for the ST, one with the maximum MFR that the experimental test bench can provide to study Mach similarity, and another with the maximum scaled MFR that the RT can manage that permits to simulate Reynolds similarity. Boundary conditions for the VGT60 case can be seen in Table 2, where ST_{Max} study was linked to the RT_{Ma} one, showing that RT had about one-ninth of the MFR that ST presented. The imposed inlet temperature for each studied case was the same, assuming an adiabatic behavior on the turbine. Figure 3 shows that for both RT simulated cases, a good agreement with the experimental results was found, being within their confidence interval.

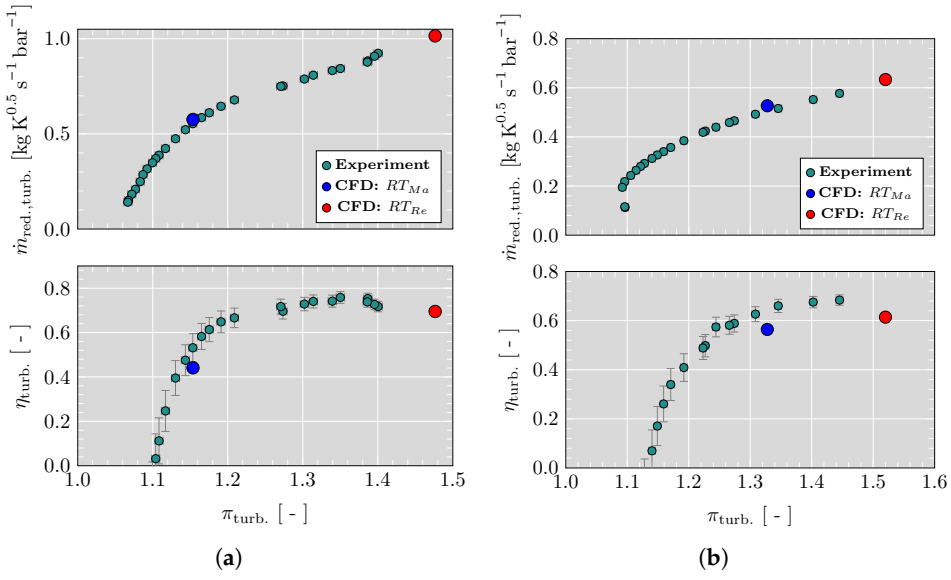

Figure 3. Real turbine map at 3890 rpm/K$^{0.5}$. (**a**) VGT60. (**b**) VGT30.

Table 2. Boundary conditions: VGT60.

	ST_{Exp}	ST_{Max}	RT_{Ma}	RT_{Re}
m [kg · s^{-1}]	0.183	0.320	0.0365	0.062
m_{red} [kg · K · s^{-1} · bar^{-1}]	3.160	5.198	0.577	0.736
$p_{tot,inlet}$ [bar]	1.073	1.141	1.175	1.560
$p_{stat,outlet}$ [bar]	1	1	1	1
$T_{tot,inlet}$ [K]	343.15	343.15	343.15	343.15
μ [N · s · m^{-2}]	1.855×10^{-5}	1.855×10^{-5}	1.855×10^{-5}	1.855×10^{-5}
Re [−]	1.269×10^{5}	2.219×10^{5}	0.759×10^{5}	1.289×10^{5}
I [−]	0.1	0.1	0.04	0.04
l [m]	0.01	0.01	0.003	0.003

For the case of the VGT30, a lower mass flow rate was obtained for the scaled turbine than that obtained for a wider vane opening. The method of conducting simulations was the same as in VGT60, but obtaining higher pressure values at the inlet of the turbine for the Mach similarity than in the other opening, which can be observed in Figure 3b looking at the PR of the turbine. The whole data used for these simulations is shown in Table 3.

Table 3. Boundary conditions: VGT30.

	ST_{Exp}	ST_{Max}	RT_{Ma}	RT_{Re}
m [kg · s^{-1}]	0.141	0.320	0.0385	0.0484
m_{red} [kg · K · s^{-1} · bar^{-1}]	2.396	4.738	0.526	0.575
$p_{tot,inlet}$ [bar]	1.086	1.252	1.357	1.560
$p_{stat,outlet}$ [bar]	1	1	1	1
$T_{tot,inlet}$ [K]	343.15	343.15	343.15	343.15
μ [N · s · m^{-2}]	1.855×10^{-5}	1.855×10^{-5}	1.855×10^{-5}	1.855×10^{-5}
Re [−]	0.978×10^{5}	2.219×10^{5}	0.801×10^{5}	1.007×10^{5}
I [−]	0.1	0.1	0.04	0.04
l [m]	0.01	0.01	0.003	0.003

3. Results

Once the boundary conditions and solver configuration were defined, a functional mesh was developed, and its independence was checked, then the CFD model of the scaled turbine was ready to be simulated for validation. A 3D study focusing on the flow patterns in the volute and stator of the turbine was then performed in the previously referred commercial code from *STAR-CCM+* . This study searched for validation of the models for the two studied vane openings, checking the limitations due to the lack of rotor in the ST.

In Figure 4, there can be seen a view at the midspan of the height of the vanes for both ST and RT. Velocity contours are shown through the inlet scroll and the stator with its vanes. Additionally, the space where the rotor would be placed is represented, although it consists of a sink in the ST model. A detailed view of the vanes V7 and V8 is shown and analyzed since those are the ones that are less distorted by any element such as the volute tongue or the screws. However, to check the validity not only for the not distorted vanes but also for those affected by the screws that are not replicated in ST, an analysis of pressure coefficient is performed over V5 and V6, since those two vanes have a screw downstream and upstream, respectively.

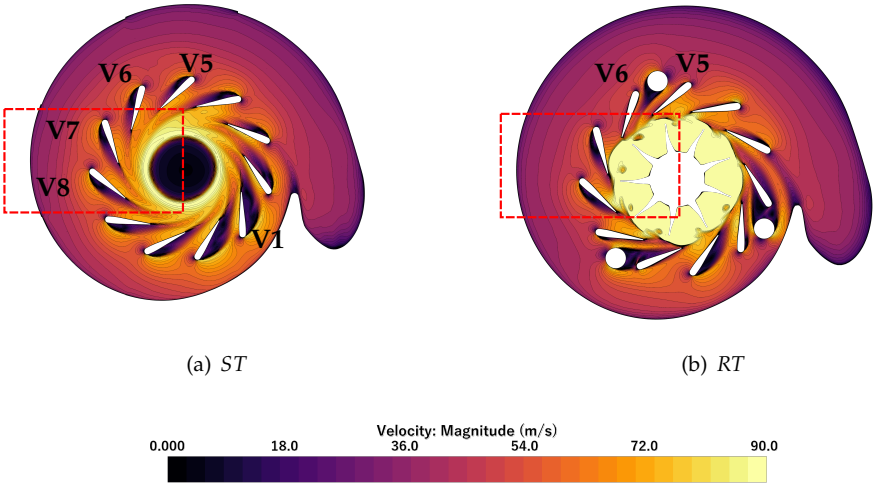

(a) *ST* (b) *RT*

Figure 4. Global velocity distribution at stator midspan. ST and RT; VGT60; 0.5 mm tip height.

3.1. Validation

The flow suffers from more significant acceleration with a narrow passage between vanes, justifying the implementation of the stator despite the losses attached to its usage. Mach number in the passages is, according to Figure 5, about 0.3 on the SS of the vanes at the same time that, on the PS, a detachment bubble can be seen in both ST and RT. On the SS, the blockage effect induced by the impeller is similar to the one that appears in the rotor-less turbine, meaning that the effect of the rotor over the stator reduces its importance when the stator has a broader opening. The lack of rotor favored the appearance of a higher velocity region when compared to the case equipped with the rotor, since the mere presence of the blades provoked losses that reduced velocity after the vane TE.

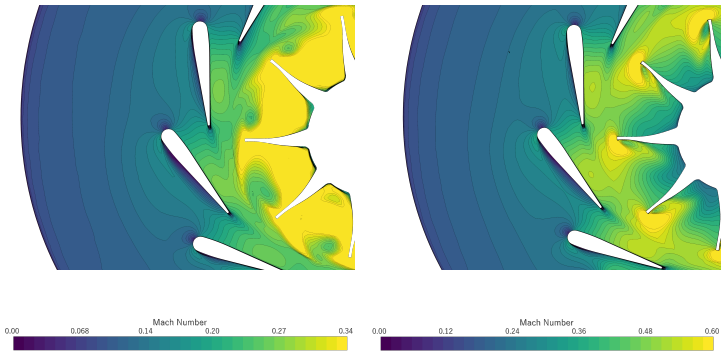

(**a**) RT_{Ma} (**b**) RT_{Re} with extended color scale

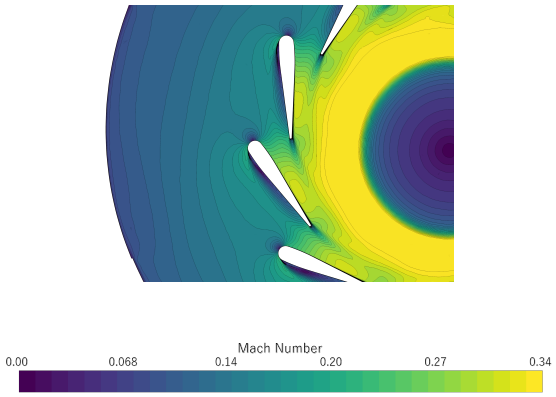

(**c**) *ST*

Figure 5. Mach number distribution at stator midspan. ST and RT; VGT60; 0.5 mm tip height.

For the closest vane, the channel position studied appears to have the highest acceleration. With this opening, the throat of the channel linked the TE on the PS of one vane with the LE on the SS of the next one. Thus, the acceleration happens toward the throat, consequently at the end of the PS having no detachment at first sight. However, taking a detailed view, as in Figure 6, different phenomena can be seen: a stagnation point perfectly aligned with the vane chord at its LE. In addition, when the flow approached the throat, it gradually accelerated in a smooth way until reaching the throat. Then, the flow suffered a substantial increase in Mach number over the SS of each vane, up to a maximum of about 0.45 Mach for the cases with equal Mach and 0.6 in the RT_{Re} case. The flow slowed down from half-chord to the TE, which constitutes a throat with the subsequent vane. The contours of the three compared cases are very similar indistinctly from their numerical values, increasing the trend whereby the closer the position, the more independent the stator performance becomes from the rotor. The interaction between rotor and stator decreases, and the ST simulation is more accurate the closer the vane opening is.

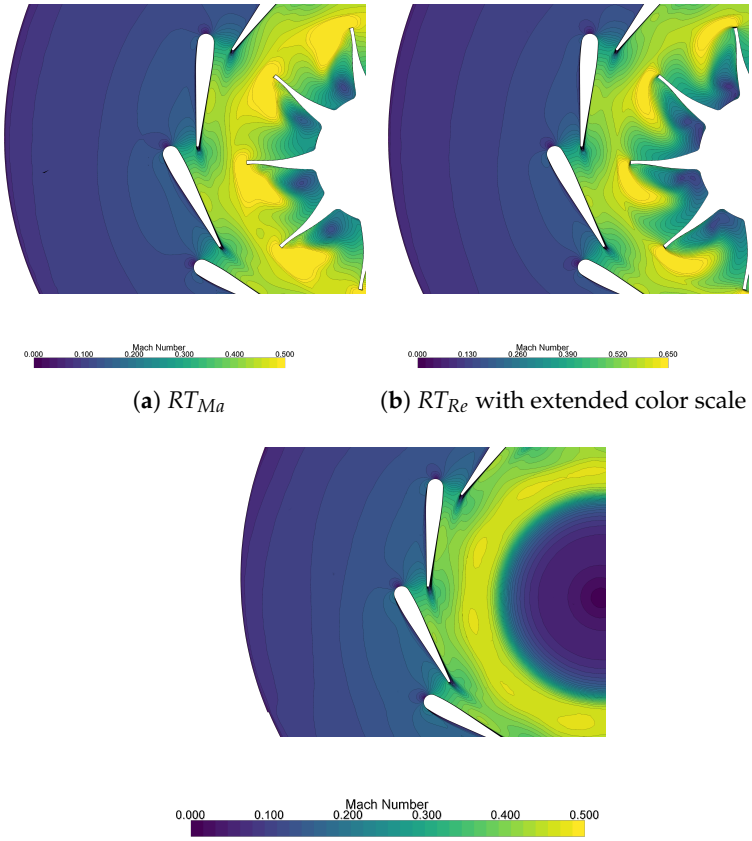

(**a**) RT_{Ma} (**b**) RT_{Re} with extended color scale

(**c**) ST

Figure 6. Mach number distribution at stator midspan. ST and RT; VGT30; 0.5 mm tip height.

After observing contours of flow patterns for each vane opening, which allows us to obtain an idea of how valid information from CFD simulations can be, data can be extracted for its processing. Pressure coefficients from different vanes were analyzed and compared, applying Equation (1) to vanes both free of distortion elements in their surroundings (**V7** and **V8**) and vanes that in RT were supposed to be affected by the screws with their analogs in the ST (**V5** and **V6**).

$$C_p = \frac{p - p_\infty}{\frac{1}{2} \cdot \rho_\infty \cdot V_\infty^2} \tag{1}$$

Data from VGT60, which can be seen in Figure 7 show, in general, a good agreement for the entire chord in both PS and SS. On the one hand, for **V8**, where there were no screws interfering with the vane, C_p distribution on the SS represents the blockage effect, showing a region of higher speed between 60% and 80% of the chord. Mach contours plotted at Figure 5 show the same region. Data between cases collide in the suction peak region in a single line. On the other hand, **V5** has its PS affected by a screw, and this side of the vane does not match that of the ST; however, the whole SS and suction peak are well represented. Right after the screw, the flow is slowed down by the screw (placed at approximately 30% of the chord). When passing next to it, there is a tendency to accelerate the flow due to a nozzle effect between the screw and the vane itself. Finally, in **V6**, which is affected on its SS by the screw, the distortion generated in the flow travels downstream from the scroll, having an impact on its PS, too. However, the primary effect appears only on the first quarter of the vane (on both sides), and after that, the coincidence between RT and ST is nearly perfect. With this data, it can be assured that the studied vane for the ST represented the same effects as the already validated turbine. Hence, the model is valid for studying effects that would take place on the experimental rig when tested.

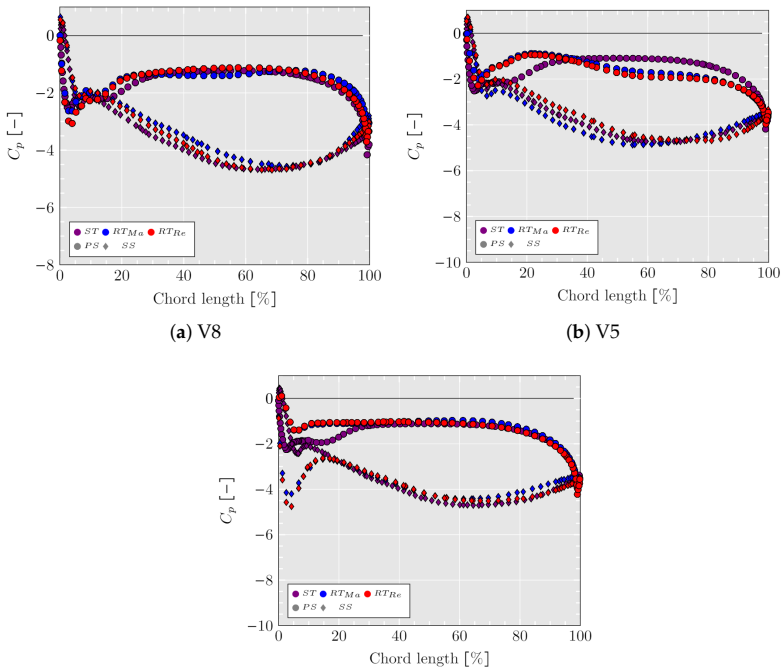

(**a**) V8 (**b**) V5

(**c**) V6

Figure 7. C_p for each studied vane. ST and RT; VGT60; 0.5 mm tip height. In the figure, legend colors stand for each case, while shapes in gray determine each of the vane faces.

The VGT30 case was also analyzed for vanes which are both affected and not by elements on the volute. Figure 8 shows how **V8** had a C_p near 0 for most of the PS after the initial distortion due to the stagnation point previously observed in Figure 6. In the ST model, this is underestimated, and the value is slightly lower, hence having a compression on that side which can be attributed to the acceleration of the flow. On the SS, the blockage effect at half chord is represented with exactitude. **V5** shows a C_p distribution that behaved similar to **V8**, but PS shows a more accentuated deceleration for the first 20% of the chord because of the presence of the screw. The vane affected by the screw on its SS, **V6**, shows such a good agreement between models, especially on SS all along the chord. Meanwhile, on PS near LE, the effect of the screw creates a brief area of detachment, reattached after the 10% of the chord and colliding results between models. In addition, it is noticeable how C_p profiles from different VGT openings are different. Still, the variation of flow conditions did not affect these pressure coefficients much for a single position.

The study that deals with Reynolds through the clearance is remarkable from the perspective of obtaining information on how flow behaves over the tip of the vane. Different methodologies were performed to check how flow behaves between ST and RT to validate if there exists a resemblance to that behavior.

Firstly, a macroscopic behavior of the flow is depicted in Figure 9 for VGT60 and in Figure 10 for VGT30. Uniform-sized vectors are drawn at a plane that crosses the tip gap at its mid-height. RT can be noticed by the presence of the screw in the form of a blank circle in which the flow stagnates. For VGT60, there is a resemblance between how the flow crosses the vane over the gap from the pressure to suction side from mid-chord to TE. However, in the RT, the tendency of the flow to cross over the gap is higher because of the influence of the rotor. For its part, VGT30 has similar behavior, but as the trend of this whole study indicates, the resemblance between RT and ST is higher, and the impeller is less affected than for wider openings, where the stator vanes TE are closer to the rotor wheel.

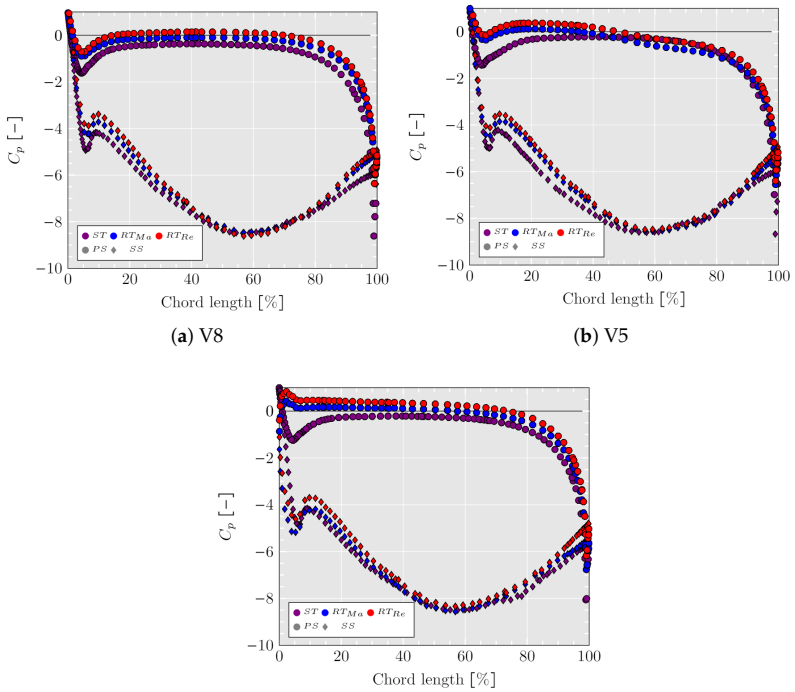

(**a**) V8 (**b**) V5

(**c**) V6

Figure 8. C_p for each studied vane. ST and RT; VGT30; 0.5 mm tip height. In the figure, legend colors stand for each case, while shapes in gray determine each of the vane faces.

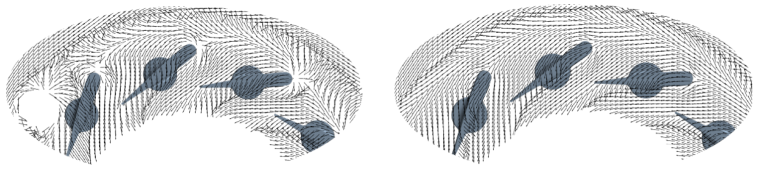

(**a**) *RT* (**b**) *ST*

Figure 9. Flow direction over the tip. ST and RT; VGT60; 0.5 mm tip height.

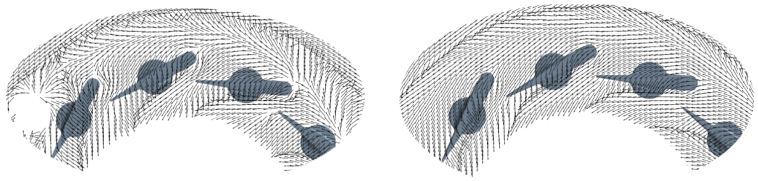

(**a**) *RT* (**b**) *ST*

Figure 10. Flow direction over the tip. ST and RT; VGT30; 0.5 mm tip height.

The distortion in the flow direction on the clearance between ST and RT can be quantified by defining a flow angle direction, ϕ. This angle is measured at the mean chord line of the vane, as shown in Figure 11a. It was measured as the direction of a particle placed in the mean chord line for every 5% of chord distance for both ST and RT. As depicted from the scheme of the vane, ϕ is non-dependent on the vane position. It is defined within its chord line, no matter which α has the referred vane. With this definition, the outlet flow angle with which the flow leaves the vane can be better understood, and the influence of not having a rotor in ST is quantified.

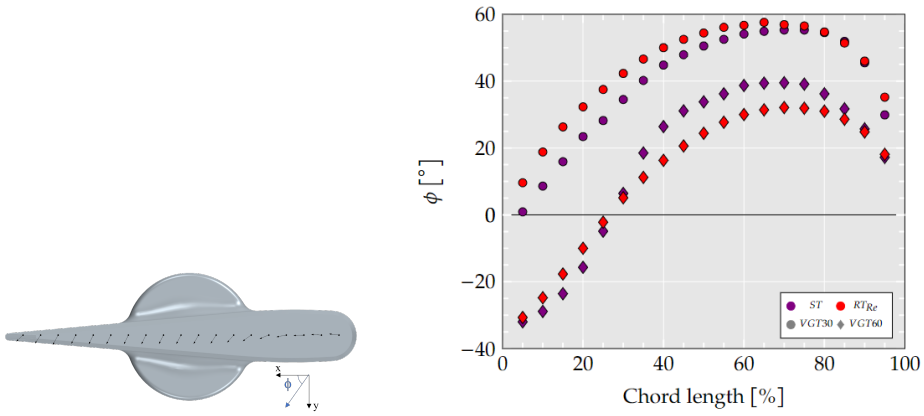

(**a**) (**b**)

Figure 11. Flow angle direction definition and comparison between different models and VGT positions. (**a**) Definition of ϕ as flow angle direction on the tip vane side. (**b**) ϕ in the mean chord line for V7. ST and RT; VGT30 and VGT60; 0.5 mm tip height. In the figure, legend colors stand for each case, while shapes in gray determine each of the vane angular positions.

In Figure 11b, the flow direction angle, ϕ for **V7** at two different vane positions, VGT30 and VGT60, can be seen. For the VGT30 case, a variation from the chord beginning exists that causes the flow in ST to be underestimated in its turning direction. However, this difference is lower than 10°, and it diminishes with chord position until reaching the same outlet flow direction as RT has. Meanwhile, the VGT60 case shows that the behavior of the flow direction for the ST case is pretty similar to the RT one. It is noticed that between 40% and 80% of the chord, there is a slight overturning in the ST simulation concerning the RT one, but, as happened in the VGT30 case, this difference is below 10°. Finally, the outlet flow angle is the same in both cases. Upon these results, it can be said that the absence of the rotor does not severely affect the flow angle over the tip, and future experiments on the ST printed model could be considered applicable to a standard turbine with a rotor.

Then, a more precise analysis can be performed studying local Reynolds numbers at different chord percentages vertically from the tip of the vane to the wall of the stator, these lines being placed along the chord line. In the generated plots (where h is the tip height and z is the height at which data are taken in the tip gap), the vertical axis represents the clearance, dimensionless with the total height of the gap to compare the original size from RT with the scaled one. In contrast, the horizontal axis evaluates local Reynolds number instead of just velocity due to the viscous nature of the flow in the clearance. Visual representation of the local Reynolds (Equation (2)) in the tip can be seen in Figure 12 for VGT60. In the first quarter of the chord, the agreement between the scaled turbine and the Reynolds similarity model was high, and even the shape of the profile was the same, with a parabolic distribution. In subsequent chord percentages, there are some discrepancies between models, although Re values do fit between ST and RT_{Re}. For each plotted case, Mach similarity obtained lower Re values, as is expected to happen, discarding this similarity to be the optimum for near-wall analysis.

$$Re_{local} = \frac{\rho_z \cdot u_z \cdot h}{\mu_z} \tag{2}$$

Tip Reynolds performance in VGT30, shown in Figure 13, reveals some particularities. The LE closest area (10% chord) has higher Re for RT_{Re} because of the stagnation point and how its turbulent effect distorts the flow. ST shows good agreement with Re similarity cases, having similar profile shapes for the ongoing points of the chord length. However, Mach similarity shows an underestimation of local Reynolds, as happened for a broader

vane position in VGT60; this causes Mach similarity to be disregarded for subsequent tip clearance flow analysis.

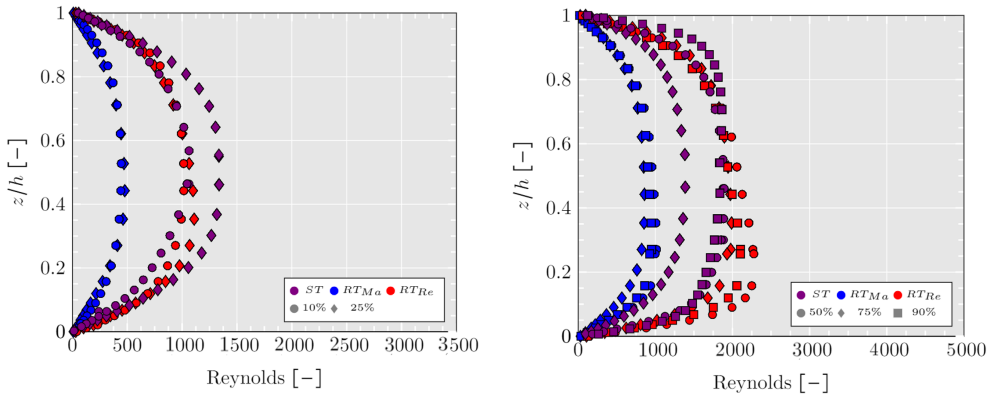

(**a**) At 10% chord and 25% chord (**b**) At 50%, 75%, and 90% chord

Figure 12. Local Reynolds number distribution in the clearance. ST and RT; VGT60; 0.5 mm tip height. In the figure, legend colors stand for each case, while shapes in gray determine each of the chord positions where data are taken.

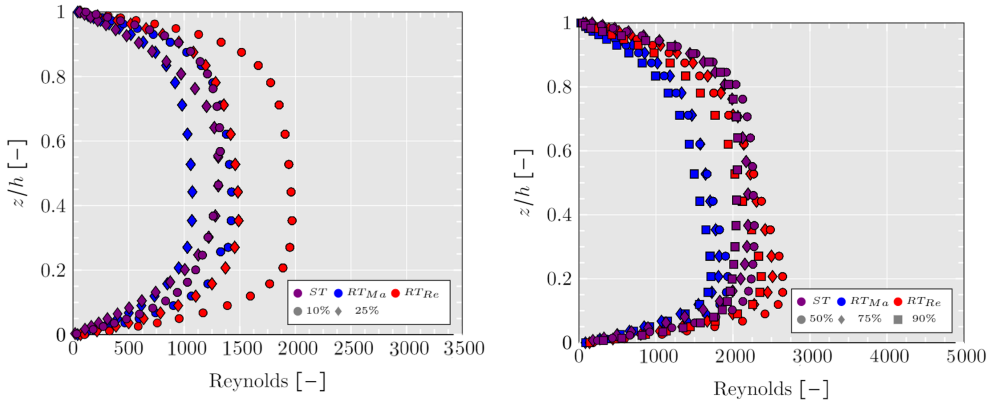

(**a**) At 10% chord and 25% chord (**b**) At 50%, 75%, and 90% chord

Figure 13. Local Reynolds number distribution in the clearance. ST and RT; VGT30; 0.5 mm tip height. In the figure, legend colors stand for each case, while shapes in gray determine each of the chord positions where data are taken.

3.2. Gap Height Variation

Having shown that ST resembles flow behavior appropriately through the gap (when the tip-to-blade height ratio is similar), and taking into account that the modular printed model had two different gap heights, we can study how it affects the variation of the gap on the tip leakage and flow behavior. This comparison is performed with the Reynolds similarity case, since it is the one that showed better agreement with the RT case when compared in previous analysis.

The leakage vortex varies with both VGT position and gap height, as shown in Figure 14. For the closest position, VGT30, it can be seen how different the vortex is for the 0.5 mm gap in the upper image from the 1.5 mm gap. On SS, there are two generated vortexes, one at mid-chord and the second at the TE; especially for the 1.5 mm gap case, this second vortex is of greater magnitude, affecting the flow that is delivered to the impeller and creating more significant losses. At VGT60, the situation described by Spence et al. [41] happened, where a first vortex is created on the PS and then the flow is sucked back through the gap to the SS, creating a vortex of greater magnitude in the greater clearance case. However, for the widest opening nozzle position, VGT80, it was found that a greater

gap diminished the suction effect generated by the PS detachment bubble, observed in [32], thus having lower tip leakage and losses in the vane faces. If volumetric mass flow is calculated through the clearance and normalized with the volume between vane and stator wall, the mass flow ratio through the 0.5 mm gap is higher than the one passing over the 1.5 mm gap. For VGT30, the ratio between these values for different gaps is just 1.05 times greater with the smaller gap, but for greater openings, this ratio rises up to 1.45 for VGT80, meaning that proportionally there are higher tip leakages through smaller gaps, especially for highly opened nozzle positions. This way, it can be said that for extreme closed positions, the importance of reducing the clearance height is more important, since it would reduce the TE vortex and subsequent losses.

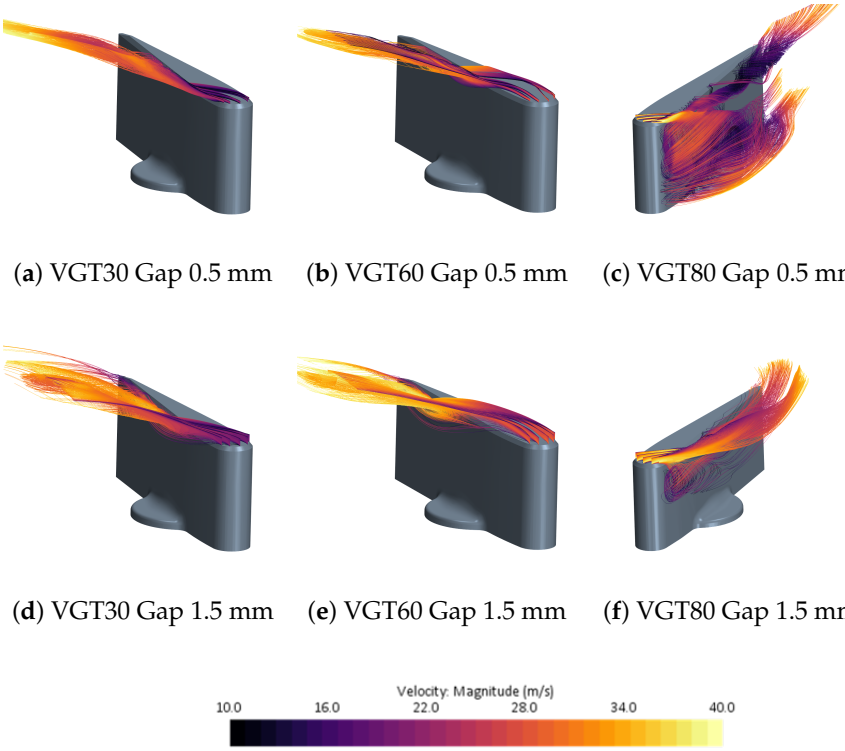

(**a**) VGT30 Gap 0.5 mm (**b**) VGT60 Gap 0.5 mm (**c**) VGT80 Gap 0.5 mm

(**d**) VGT30 Gap 1.5 mm (**e**) VGT60 Gap 1.5 mm (**f**) VGT80 Gap 1.5 mm

Figure 14. Tip gap vortex streamlines for two gap configurations and three vane openings. ST; VGT30, VGT60, and VGT80; 0.5 and 1.5 mm tip height.

Another way of looking at this tip leakage interaction is by studying different planes through the vane, as in Figure 15. This study was performed on the vanes of the ST for the two different gap heights designed. In this case, velocity convoluted vectors are displayed to make it possible to check vortexes formation and tip leakages all along the vane. However, a detailed view shows that the most significant area of the vane is the TE. For that reason, studied planes are those placed at the 60% and 80% of the chord.

For the narrowest vane nozzle position, in Figure 15a, it can be seen how the higher clearance mainly affects the TE vortex, with higher tip leakages from PS to SS enlarging the vortex and blocking part of the vane, thus increasing losses.

Other phenomena can be observed with a broader position, such as VGT60, represented in Figure 15b. As the blade loading for this opening is lower than in the VGT30 case, there is a more negligible suction effect through the gap. For the 1.5 mm gap, the TE vortex tends to be of lower magnitude and more stuck to the vane wall than what happens in the 0.5 mm gap. This result reinforces the crucial importance of reducing the clearance height if the turbine is expected to work at narrow openings, as depicted in Figure 14.

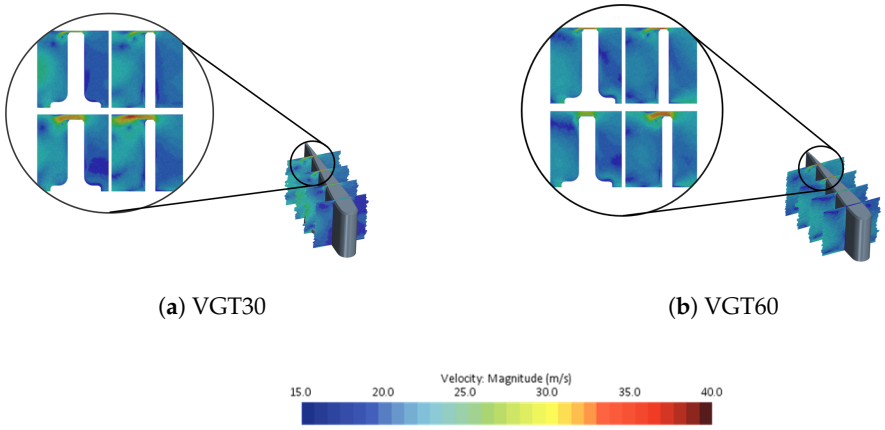

(**a**) VGT30 (**b**) VGT60

Figure 15. Velocity convoluted vectors for different chord lengths. ST; VGT30 and VGT60; 0.5 and 1.5 mm tip height.

4. Conclusions

The analysis and validation of a tool capable of linking an enlarged scaled model of a turbine without rotor and a conventional radial turbine is the main objective of this study. The aim is to check the flow behavior in the volute and stator of the scaled model and compare it with what is predicted in a real turbine model. The model of the real turbine was validated with general outputs, those that can be measured in a conventional turbocharger test bench. The computational model of the scaled, rotor-less turbine matches the performance of the real-sized turbine model. This study set the basis of a work methodology that would allow studying flow patterns. Experimental testing of the scaled model would conclude the accuracy of the predictions in the inner channels of the stator and tip gap for different configurations, since it was concluded that the lack of rotor has little impact in flow patterns in the stator vanes. The current turbine measuring methodology mainly involves measuring inlet and outlet conditions, while the scaled printed model alongside the presented computational modeling would allow much better experimental results.

By analyzing the results, the interaction between rotor and stator was quantified, that is, the flow at the stator that became affected by the presence of the rotor is higher as the channel between vanes is broader. However, it was shown how, for a wide variation of VGT positions, the lack of rotor does affect the analysis on flow behavior through the stator. This has implications in future studies focusing on the stator of a turbine, since discarding the rotor in numerical simulations saves a huge amount of computational cost. The complexity and cost that entail the implementation of a rotor in the 3D printed model make it necessary to check the interaction between the stator and the rotor. For the two vane openings shown in this study, VGT30 and VGT60, the consistency between the scaled and the real models is high in the stator region. Under these results, further analysis can be performed on how other characteristics of the real turbine affected the performance of the stator, for example, the screws that cross the stator in the spanwise direction. Another point of interest could be how the pressure coefficient had significant discrepancies between different nozzle openings, but not so much between different flow conditions, as the different similarities simulated showed.

Regarding the study of the clearance left between the vane tip and the upper stator wall, it was justified that keeping the Reynolds number is a valuable way to represent the phenomena, as the CFD model of the real turbine does. Thus, it was shown how outlet flow angle through the tip had little variation whether there is a rotor or not downstream from the stator vanes. Some discrepancies appeared when studying local Reynolds number in the tip, but taking into account the viscous nature of the flow over it and how much could it be affected by slight differences, such as the tip vane shape itself, the results showed good

agreement having similar Reynolds number at the same chord percentages and similar distribution shapes through the length of the gap.

Moreover, two different clearances heights were simulated and compared for the scaled model, showing that this gap should be minimized to decrease tip leakage losses. This action gains interest if the desire is to work under small nozzle openings, and its influence is shown to be lower for broader positions.

Author Contributions: Conceptualization, J.A.L.-C. and A.O.T.; methodology, J.A.L.-C. and N.H.-G.; software, J.A.L.-C.; validation, A.O.T., J.A.L.-C. and N.H.-G.; formal analysis, J.R.S.; investigation, J.A.L.-C. and N.H.-G.; resources, A.O.T. and N.H.-G.; data curation, J.A.L.-C.; writing—original draft preparation, J.A.L.-C., A.O.T. and N.H.-G.; writing—review and editing, J.R.S.; visualization, J.A.L.-C.; supervision, J.R.S.; project administration, J.R.S. and A.O.T. All authors have read and agreed to the published version of the manuscript.

Funding: This research work was supported by Grant PDC2021-120821-I00, funded by MCIN/AEI/10.13039/501100011033 and by European Union NextGeneration EI/PRTR.

Institutional Review Board Statement: Authors choose to exclude this statement since they consider that this study does not require ethical approval. There were no humans or animals involved in the study.

Informed Consent Statement: Authors choose to exclude this statement since there were no humans involved in the study.

Data Availability Statement: The data that support the findings of this study are available from the corresponding author upon reasonable request.

Conflicts of Interest: The authors declare no conflicts of interest.

Abbreviations

The following abbreviations are used in this manuscript:

CFD	Computational Fluid Dynamics
EU	European Union
MFR	Mass Flow Rate
SS	Suction Side
PS	Pressure Side
RT	Real Turbine
ST	Scaled Turbine
LE	Leading Edge
TE	Trailing Edge
PR	Pressure Ratio
RANS	Reynolds Average Navier–Stokes
VGT	Variable Geometry Turbine
Roman Letters	
Ma	Mach Number
Re	Reynolds Number
$\dot{m}$	Mass Flow
$\dot{m}_{red.}$	Reduced Mass Flow
p	Pressure
I	Turbulence Intensity
l	Turbulence Length Scale
h	Tip Gap Height
Greek Letters	
α	Stator Blade Angle
η	Efficiency
μ	Dynamic Viscosity
π	Corresponding Pressure Ratio
ϕ	Flow Angle

Subscripts and Superscripts

in	Turbine Inlet Section
Ma	Mach Similarity
red.	Reduced Numbers
Re	Reynolds Similarity
rel.	Relative Value
s	Static Conditions
surf.	Stator Vane or Rotor Blade Surface
tot	Total or Stagnation Conditions
t, *s*	Total-To-Static Value

References

1. Yaumi, A.L.; Bakar, M.A.; Hameed, B. Recent advances in functionalized composite solid materials for carbon dioxide capture. *Proc. ICE Energy* **2017**, *124*, 461–480. [CrossRef]
2. Williams, M.; Minjares, R. *A Technical Summary of Euro 6-VI Vehicle Emission Standards*; International Council for Clean Transportation (ICCT): Washington, DC, USA, 2016; pp. 1–17.
3. *Commission Regulation (EU) 2016/427 of 10 March 2016 Amending Regulation (EC) No. 692/2008 as Regards Emissions from Light Passenger and Commercial Vehicles (Euro 6), 2016*; European Union: Maastricht, The Netherlands, 2016.
4. Praveena, V.; Martin, M. A review on various after treatment techniques to reduce NOx emissions in a CI engine. *J. Energy Inst.* **2018**, *91*, 704–720. [CrossRef]
5. Joshi, M.; Shaver, G.; Vos, K.; McCarthy, J.; Farrell, L.A. Internal exhaust gas recirculation via reinduction and negative valve overlap for fuel-efficient aftertreatment thermal management at curb idle in a diesel engine. *Int. J. Engine Res.* **2021**, *23*, 11. [CrossRef]
6. Pla, B.; Bares, P.; Sanchis, E.; Aronis, A. Ammonia injection optimization for selective catalytic reduction aftertreatment systems. *Int. J. Engine Res.* **2021**, *22*, 2169–2179. [CrossRef]
7. Cheng, L.; Dimitriou, P.; Wang, W.; Peng, J.; Aitouche, A. A novel fuzzy logic variable geometry turbocharger and exhaust gas recirculation control scheme for optimizing the performance and emissions of a diesel engine. *Int. J. Engine Res.* **2020**, *21*, 1298–1313. [CrossRef]
8. Sindhu, R.; Rao, G.P.; Murthy, K. Effective reduction of NOx emissions from diesel engine using split injections. *Alex. Eng. J.* **2018**, *57*, 1379–1392. [CrossRef]
9. Pla, B.; Piqueras, P.; Bares, P.; Aronis, A. Simultaneous NOx and NH 3 slip prediction in a SCR catalyst under real driving conditions including potential urea injection failures. *Int. J. Engine Res.* **2021**, *23*, 14680874211007646.
10. Inaba, K.; Ojima, Y.; Masuko, Y.; Kobashi, Y.; Shibata, G.; Ogawa, H. Thermal efficiency improvement with super-charging and cooled exhaust gas recirculation in semi-premixed diesel combustion with a twin peak shaped heat release. *Int. J. Engine Res.* **2019**, *20*, 80–91. [CrossRef]
11. Kunanoppadon, J. Thermal Efficiency of a Combined Turbocharger Set with Gasoline Engine. *Am. J. Eng. Appl. Sci.* **2010**, *3*, 342–349. [CrossRef]
12. Mahmoudi, A.R.; Khazaee, I.; Ghazikhani, M. Simulating the effects of turbocharging on the emission levels of a gasoline engine. *Alex. Eng. J.* **2017**, *56*, 737–748. [CrossRef]
13. Enisu, M.; Terakawa, Y.; Ibaraki, S. Mitsubishi turbocharger for lower pollution cars. *Mitsubishi Heavy Ind. Tech.* **2004**, *41*, 1–3.
14. Germanand, J.; Isenstadt, A. Downsized Boosted Gasoline Engines. *Int. Counc. Clean Transp.* **2016**, *22*, 1–13.
15. Serrano, J.; Piqueras, P.; la Morena, J.D.; Gómez-Vilanova, A.; Guilain, S. Methodological analysis of variable geometry turbine technology impact on the performance of highly downsized spark-ignition engines. *Energy* **2021**, *215*, 119122. [CrossRef]
16. Benajes, J.; Novella, R.; Gomez-Soriano, J.; Barbery, I.; Libert, C. Advantages of hydrogen addition in a passive pre-chamber ignited SI engine for passenger car applications. *Int. J. Engine Res.* **2021**, *45*, 13219–13237. [CrossRef]
17. Yip, H.L.; Srna, A.; Yuen, A.C.Y.; Kook, S.; Taylor, R.A.; Yeoh, G.H.; Medwell, P.R.; Chan, Q.N. A Review of Hydrogen Direct Injection for Internal Combustion Engines: Towards Carbon-Free Combustion. *Appl. Sci.* **2019**, *9*, 4842. [CrossRef]
18. Kerviel, A.; Pesyridis, A.; Mohammed, A.; Chalet, D. An Evaluation of Turbocharging and Supercharging Options for High-Efficiency Fuel Cell Electric Vehicles. *Appl. Sci.* **2018**, *8*, 2474. [CrossRef]
19. European Commission. *Hydrogen Energy and Fuel Cells: A Vision for Our Future*; European Commission: Karlsruhe, Germany, 2003.
20. Suhrmann, J.F.; Peitsch, D.; Gugau, M.; Heuer, T. On the Effect of Volute Tongue Design on Radial Turbine Performance. *Turbo Expo Power Land Sea Air* **2012**, *8*, 891–901. [CrossRef]
21. Cravero, C.; Leutcha, P.J.; Marsano, D. Simulation and Modeling of Ported Shroud Effects on Radial Compressor Stage Stability Limits. *Energies* **2022**, *15*, 2571. [CrossRef]
22. Galindo, J.; Serrano, J.R.; Garcia-Cuevas, L.M.; Medina, N. Using a CFD analysis of the flow capacity in a twin-entry turbine to develop a simplified physics-based model. *Aerosp. Sci. Technol.* **2021**, *112*, 106623. [CrossRef]
23. Mehrnia, S.; Miyagawa, K.; Kusaka, J.; Nakamura, Y. Radial turbine optimization under unsteady flow using nature-inspired algorithms. *Aerosp. Sci. Technol.* **2020**, *103*, 105903. [CrossRef]

24. Marsan, A.; Moreau, S. Analysis of the flow structure in a radial turbine. In Proceedings of the 11th European Conference on Turbomachinery Fluid Dynamics & Thermodynamics, Madrid, Spain, 23–25 March 2015.
25. Maki, H.; Mori, Y. On the Study of the Flow through an Impeller of Mixed and Inward-Flow Radial Turbines: 3rd Report, Interference with the Flow from the Circular Nozzle. *Jpn. Soc. Mech. Eng.* **1973**, *16*, 81–92. [CrossRef]
26. Binder, N.; Guyaderand, S.L.; Carbonneau, X. Analysis of the Variable Geometry Effect in Radial Turbines. *ASME. J. Turbomach.* **2012**, *134*, 041017. [CrossRef]
27. Zhu, C.; Shao, W.Y.; Ma, Z.Y.; Lv, G.C.; Wang, X.F. Investigation on Interaction between Geometry and Performance and Design of S-CO_2 Radial Inflow Turbine's Vaneless Inlet Volute. In Proceedings of the Fourth Chinese International Turbomachinery Conference (CITC 2020), Nanchang, China, 10–13 April 2020.
28. Giersch, T.; Hönisch, P.; Beirow, B.; Kühhorn, A. Forced response analyses of mistuned radial inflow turbines. *J. Turbomach.* **2013**, *135*, 031034. [CrossRef]
29. Píštěk, V.; Kučera, P.; Fomin, O.; Lovska, A. Effective mistuning identification method of integrated bladed discs of marine engine turbochargers. *J. Mar. Sci. Eng.* **2020**, *8*, 379. [CrossRef]
30. Tiseira, A.; Garcia-Cuevas, L.; Inhestern, L.; Echavarria, J. Development of Choked Flow in Variable Nozzle Radial Turbines. *Int. J. Engine Res.* 2021, *in press*. [CrossRef]
31. Galindo, J.; Arnau, F.J.; Garcia-Cuevas, L.M.; Soler, P. Experimental validation of a quasi-two-dimensional radial turbine model. *Int. J. Engine Res.* **2020**, *21*, 915–926. [CrossRef]
32. Tiseira, A.; Navarro, R.; Inhestern, L.; Hervás, N. Design and Numerical Analysis of Flow Characteristics in a Scaled Volute and Vaned Nozzle of Radial Turbocharger Turbines. *Energies* **2020**, *13*, 2930. [CrossRef]
33. Sharma, S.; Garcia-Tiscar, J.; Allport, J.M.; Barrans, S.; Nickson, A.K. Evaluation of modelling parameters for computing flow-induced noise in a small high-speed centrifugal compressor. *Aerosp. Sci. Technol.* **2020**, *98*, 105697. [CrossRef]
34. Pan, L.; Yang, M.; Murae, S.; Sato, W.; Shimohara, N.; Yamagata, A. Influence of tip clearance distribution on blade vibration of vaneless radial turbine. *Proc. Inst. Mech. Eng. Part J. Automob. Eng.* **2022**, *236*, 1007–1018. [CrossRef]
35. Serrano, J.R.; Gil, A.; Navarro, R.; Inhestern, L.B. Extremely low mass flow at high blade to jet speed ratio in variable geometry radial turbines and its influence on the flow pattern: A CFD analysis. In Proceedings of the ASME Turbo Expo 2017: Turbomachinery Technical Conference and Exposition, Charlotte, NC, USA, 26–30 June 2017.
36. Dufour, G.; Carbonneau, X.; Arbez, P.; Cazalbou, J.B.; Chassaing, P. Mesh-generation parameters influence on centrifugal compressor simulation for design optimization. In Proceedings of the Heat Transfer Summer Conference, Charlotte, NC, USA, 11–15 July 2004; Volume 46911, pp. 609–617.
37. Menter, F.R.; Kuntz, M.; Langtry, R. Ten years of industrial experience with the SST turbulence model. *Turbul. Heat Mass Transf.* **2003**, *4*, 625–632.
38. Baar, R.; Biet, C.; Boxberger, V.; Mai, H.; Zimmermann, R. New evaluation of turbocharger components based on turbine outlet temperature measurements in adiabatic conditions. In Proceedings of the ISROMAC-15, Honolulu, HI, USA, 24–28 February 2014; pp. 24–28.
39. Zimmermann, R.; Baar, R.; Biet, C. Determination of the isentropic turbine efficiency due to adiabatic measurements and the validation of the conditions via a new criterion. *Proc. Inst. Mech. Eng. Part J. Mech. Eng. Sci.* **2018**, *232*, 4485–4494. [CrossRef]
40. Serrano, J.R.; Tiseira, A.; Garcia-Cuevas, L.M.; Inhestern, L.B.; Tartoussi, H. Radial turbine performance measurement under extreme off-design conditions. *Energy* **2017**, *125*, 72–84. [CrossRef]
41. Spence, S.W.T.; O'Neill, J.; Cunningham, G. An investigation of the flowfield through a variable geometry turbine stator with vane endwall clearance. *Proc. Inst. Mech. Eng. Part J. Power Energy* **2006**, *220*, 899–910. [CrossRef]